

Coherent dynamics of a photon-dressed qubit

M. P. Liul,^{1,*} C.-H. Chien,^{2,*} C.-Y. Chen,² P. Y. Wen,³ J. C. Chen,^{2,4}
Y.-H. Lin,^{2,4} S. N. Shevchenko,^{1,†} Franco Nori,^{5,6,7} and I.-C. Hoi^{8,2,‡}

¹*B. Verkin Institute for Low Temperature Physics and Engineering, Kharkov 61103, Ukraine*

²*Department of Physics, National Tsing Hua University, Hsinchu 30013, Taiwan*

³*Department of Physics, National Chung Cheng University, Chiayi 621301, Taiwan*

⁴*Center for Quantum Technology, National Tsing Hua University, Hsinchu 30013, Taiwan*

⁵*Theoretical Quantum Physics Laboratory, Cluster for Pioneering Research, RIKEN, Wakoshi, Saitama 351-0198*

⁶*Quantum Computing Center, RIKEN, Wakoshi, Saitama 351-0198, Japan*

⁷*Department of Physics, The University of Michigan, Ann Arbor, MI 48109-1040, USA*

⁸*Department of Physics, City University of Hong Kong,*

Tat Chee Avenue, Kowloon, Hong Kong SAR, China

(Dated: May 30, 2023)

We consider the dynamics and stationary regime of a capacitively shunted transmon-type qubit in front of a mirror. The qubit is affected by probe and dressing signals. By varying the parameters of these signals and then analyzing the probe signal (reflected by the “atom plus mirror” system), it is possible to explore the system dynamics, which can be described by the Bloch equation. The obtained time-dependent occupation probabilities are related to the experimentally measured reflection coefficient. The study of this type of dynamics opens up new horizons for better understanding the “qubit plus mirror” circuit properties and the underlying physical processes, such as Landau-Zener-Stückelberg-Majorana transitions.

I. INTRODUCTION

Topics related to quantum computing are attracting considerable attention [1–5]. One of the most promising building blocks of such devices are superconducting qubits (see, e.g., [6–8]). These can be operated at nanosecond scales with millisecond coherence times [9], are controlled by microwaves and have lithographic scalability [10]. Therefore, investigations of superconducting qubits could help in the development of quantum computers.

A superconducting qubit in a semi-infinite transmission line [11] is important for quantum electrodynamics, especially waveguide quantum electrodynamics (WQED) [12–14]. For example, in Ref. [15] it was found that a transmon qubit embedded at the end of a transmission line can amplify a probe signal with an amplitude gain of up to 7%; while a single quantum dot [16] and natural atoms [17] show the signal amplifications at much lower levels: 0.005% and 0.4%, respectively. The investigation of our system can also address interesting physics issues in WQED, including: dynamics in atom-like mirrors [18], collective Lamb shift [19], generation of non-classical microwaves [20], the dynamical Casimir effect [21], cross-Kerr effect [22], photon routing [23], probabilistic motional averaging [24], etc.

Driven quantum systems can be described in terms of Landau-Zener-Stückelberg-Majorana (LZSM) transitions [25–28]. If driven periodically, these experience interference. The corresponding LZSM interferometry is important both for studying fundamental quantum phenomena and as a convenient tool for characterizing quantum systems. The use of LZSM interferometry for controlling quantum dynamics was studied in Refs. [28–34]. Quantum logic gates can also be implemented using LZSM

dynamics [35].

In a preceding work, Ref. [36], we explored LZSM interferometry spectroscopically, i.e. in the frequency domain. Taking advantages of the strong coupling between propagating fields and qubits, as well as the ease of fabrication, circuits with superconducting qubits in front of a mirror provide a versatile platform to study the dynamics of LZSM interference, as compared with other quantum two-level systems.

The rest of the paper is organized as follows. Section II is devoted to the description of the experiment. In Sec. III the theoretical aspects of the problem are described; we introduce the Hamiltonian of the system and the equation of motion which was solved to obtain the quantities shown. Section IV presents our results: a comparison of the theory and the experiment is given; the general patterns of the system are described and explained; additional results are given in Appendix A. In Sec. V we present our conclusions.

II. EXPERIMENT

Our device consists of a transmon qubit, embedded at a distance ($L \simeq 33$ mm, where the resonant frequency corresponds to 1.84λ) of a finite quasi-one-dimensional transmission line with characteristic impedance $Z_0 \simeq 50 \Omega$, as shown in Fig. 1 (a,b). The transmission line allows the formation of standing EM waves along the transmission line, therefore, the voltage field strength experienced by the qubit can be controlled by the location of the qubit in the transmission line, as illustrated in Fig. 1(a). In principle, we could have used a short instead of an open end for the transmission line. However, this changes the boundary conditions. In particular, the phase of the

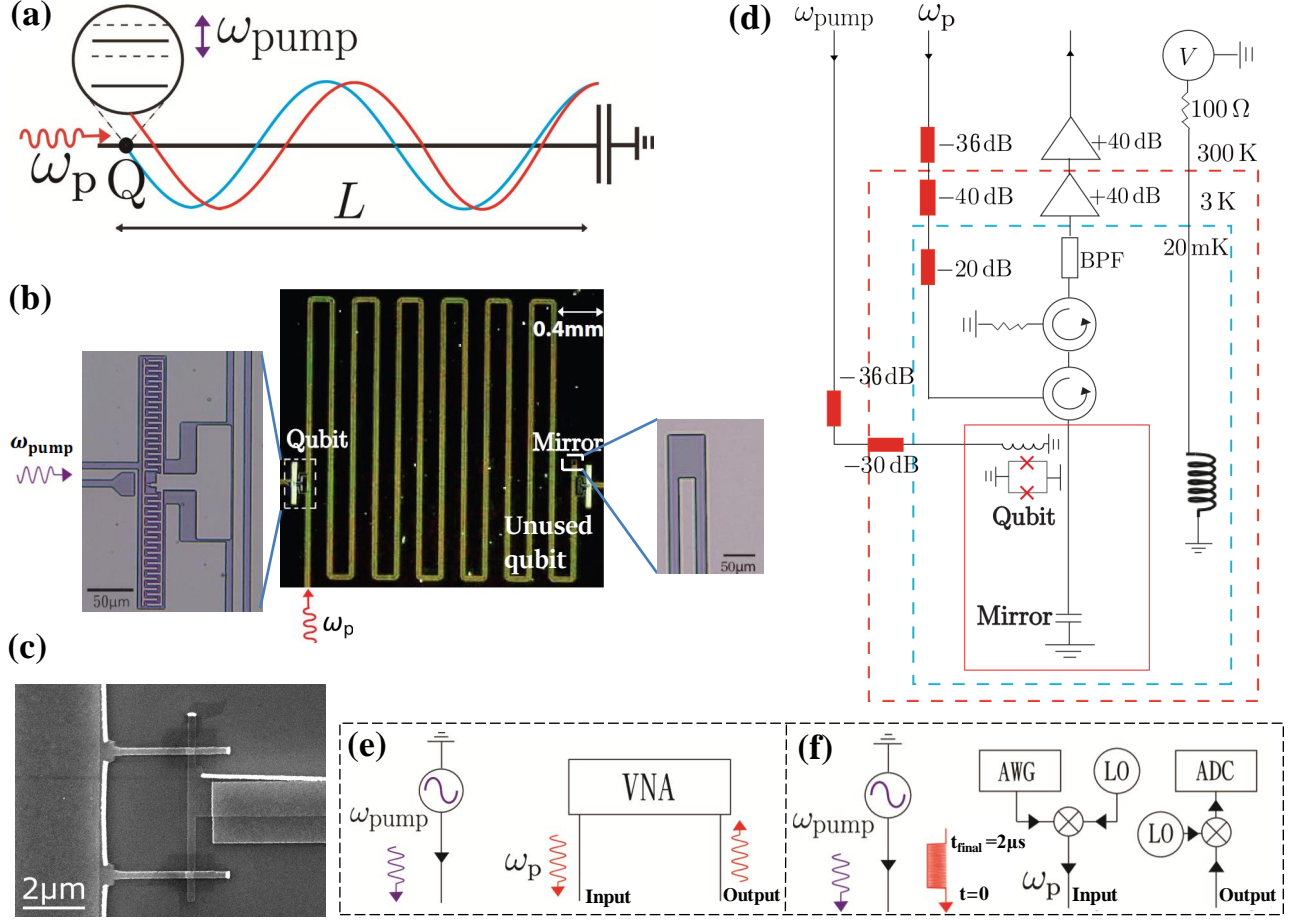


Figure 1: Device and its characterization. (a) Conceptual sketch of the device: a two-level atom, point-like object (denoted by Q), is coupled to a semi-infinite transmission line waveguide. The atom is located at a distance $L \simeq 33$ nm (1.84λ , indicated by the red curve, $1.75\lambda_{\text{node}}$, indicated by the blue curve) away from the mirror (capacitance). A pump tone with frequency ω_{pump} is applied to modulate the transition frequency of the two-level atom. A weak probe tone with frequency ω_p is applied to the atom-mirror system to measure the reflection coefficient. (b) Micrographs of the device. The magnification of the active qubit is shown to the left, where the superconducting qubit is intentionally designed to be weakly coupled to the transmission line. The weak coupling enables us to measure the temporal dynamics with a nano-second digitizer. This is the main difference between this work and a previous one [36] which focused on the stationary regime. A capacitor to ground, which creates an antinode voltage field at the end of the transmission line and acts as a mirror, is shown to the right. The transmission line ends in another qubit, which is designed for another experiment and is not participating in the experiment (because it is far detuned). (c) Contains a scanning-electron-microscope picture of the qubit dc-SQUID which enables flux tunability. (d) The experimental setup shows the probe tone and pump tone being applied to the atom-mirror system. Panels (e) Vector Network Analyzer [VNA], Signal Generator and (f) Arbitrary Waveform Generator [AWG], Local Oscillator [LO], Analog-to-Digital Converter [ADC] show the setup for Figs. 2, 3 and Figs. 4, 5, 6, 7 respectively.

incident wave acquires a π phase shift, instead of a zero phase shift. And the voltage at the end of transmission line would be at the node instead of at the antinode. Figure 1 (c) contains a scanning-electron-microscope picture of the qubit dc-SQUID which enables flux tunability. We only consider the lowest two energy levels of the transmon, and neglect all the higher levels. The energy splitting of the two-level atom is $\hbar\omega_{10}(\Phi) \approx \sqrt{8E_J(\Phi)E_C} - E_C$, with charging energy E_C (which is approximately equal to the anharmonicity), $E_C = e^2/2C_\Sigma$, where e is the elementary charge and C_Σ is the total capacitance of the transmon, and the Josephson energy E_J , which can be

tuned by the external magnetic flux Φ of a magnetic coil. The detailed measurement setup is presented in Fig. 1(d). Here ω_p is the probing frequency (indicated in red color in Fig. 1(b,e,f)), a continuous wave created by the vector network analyzer or the microwave pulse from the arbitrary wave generator; we input the continuous wave with pump frequency ω_{pump} by the RF source (indicated by purple color in Fig. 1(b,e,f)).

Parameter	Description	Value in Ref. [36]	Current value
ω_{node}	Node frequency	$2\pi \times 4.75$ GHz	$2\pi \times 4.38$ GHz
ω_{10}	Qubit frequency	$\simeq \omega_{\text{node}}$	$2\pi \times 5$ GHz
δ	Pump amplitude	$\sim 2\pi \times 0.1$ GHz	$< 2\pi \times 40$ MHz
ω_{pump}	Pump frequency	$< 2\pi \times 0.1$ GHz	$2\pi \times 1 \sim 15$ MHz
ω_{p}	Probe frequency	$\simeq \omega_{\text{node}}$	$2\pi \times 5$ GHz
Γ_1	Relaxation rate	$< 2\pi \times 5$ MHz	$2\pi \times 0.28$ MHz
Γ_ϕ	Pure dephasing rate	$\sim 2\pi \times 3$ MHz	$2\pi \times 0.61$ MHz
$\Gamma_2 = \Gamma_1/2 + \Gamma_\phi$	Decoherence rate	$\sim 2\pi \times 5.5$ MHz	$2\pi \times 0.75$ MHz

Table I: Comparison of parameters between this work and a previous one, Ref. [36].

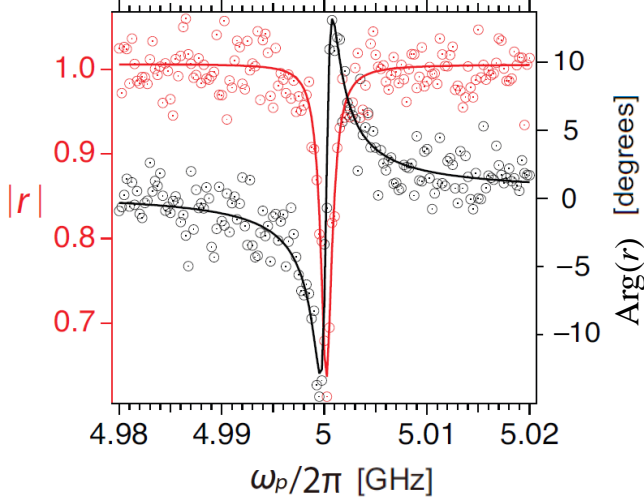


Figure 2: Reflection coefficient (magnitude response in red and phase response in black) as a function of probe frequency ω_p for a weak probe (-166 dBm), see Fig. 1(e) with pump off. Data are shown by circles and the solid curves are the fit, using a similar fitting method as in Ref. [37].

A. Characterizing the qubit by single-tone scattering with a weak probe

We characterize our qubit by a single-tone scattering with a weak probe, see Fig. 2. Fitting the magnitude and phase response of the reflection coefficient r by using the circle fit equation Eq. (1) [38] one could extract the resonant frequency ω_{10} , the relaxation rate Γ_1 and decoherence rate Γ_2 :

$$r = 1 - \frac{\Gamma_1}{\Gamma_2 + i(\omega_p - \omega_{10})}, \quad (1)$$

here r is defined as the reflected field amplitude divided by the incoming field amplitude. The extracted values are the following: $\omega_{10}/2\pi = 5$ GHz, $\Gamma_1/2\pi = 0.28$ MHz, and $\Gamma_2/2\pi = 0.75$ MHz. These parameters will be used in the theory later. Note that we assume the incoming amplitude to be the same as the reflected amplitude when the qubit is detuned. By using two-tone spectroscopy, we know that E_C/h (anharmonicity) = 220 MHz (data not shown), which is much larger than any Rabi frequency in this work, and our two-level atom assumption is valid.

From ω_{10} and E_C , we know that $E_J/h = 15.5$ GHz.

B. Reflection coefficient versus pump power and probe frequency

We apply both probe and dressing (pump) signals to the transmission line and the on-chip flux line (which modulates the transition frequency of the qubit), respectively. We then measure the reflection coefficient r in the (steady state) frequency domain, see Fig. 1(e). Both frequency and power for the pump tone and probe tone are all tunable. Here, we scan the frequency of probe ω_p , frequency of pump ω_{pump} , power of pump P_{pump} , and measure the reflection coefficient $|r|$ with a fixed power of the weak probe tone.

The results are shown in Fig. 3. In each subplot of Fig. 3, we fix the pump frequency, vary the pump power (y -axis) and probe frequency (x -axis). We see a LZSM interferometry pattern, where we clearly observe multi-photon resonances, which occur at $\omega_p - \omega_{10} \equiv \Delta\omega = k\omega_{\text{pump}}$, where k is an integer number. From the experimental and theory plots, one can calibrate the Rabi frequency and the pump power. In addition, from these plots it is possible to extract qubit parameters, such as the relaxation rate Γ_1 , pure dephasing rate Γ_ϕ , and decoherence rate Γ_2 . The parameters obtained are shown in Table I. Note that the $k = 0$ transition is observed because we tune the qubit frequency away from the node frequency, similar to Fig. 5(c) in Ref. [36]. If the qubit is at a node then a transition for $k = 0$ is not observed (see Fig. 5(b) in Ref. [36]).

As shown in Fig. 3(b), the higher pump powers allow to resolve more sidebands, visible there up to $k = \pm 5$. The experimental LZSM interferometry pattern shown in Fig. 3(a,b,c) matches very well with the theory in Fig. 3(d,e,f). Also one can see the drift on the multi-photon resonance at high power in (c), which is due to flux drift (caused by environmental background flux), because the resonance frequency is controlled by the flux. Detailed calculations are shown in Sec. III. Since we are using a weak probe, the upper-level occupation probability P_1 is low.

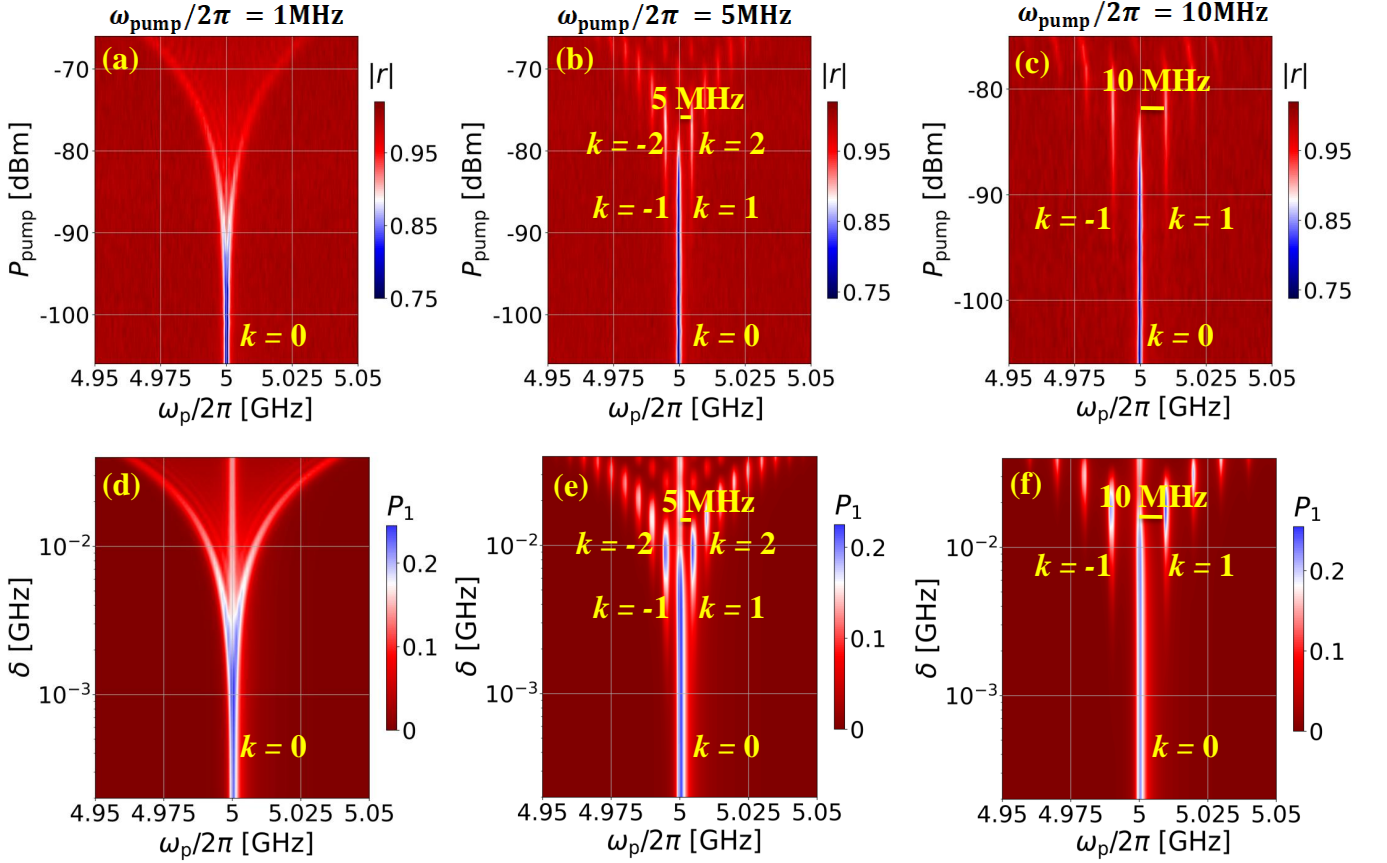


Figure 3: LZSM interferograms. These are shown via the dependence of the reflection coefficient $|r|$ on the pump power P_{pump} and probe frequency ω_p at fixed pump frequency ω_{pump} for a weak probe $P_p = -152$ dBm in the top panels (a,b,c) for the experimental measurements. While the bottom panels (d,e,f) show the theoretically calculated upper-level occupation probability P_1 as a function of the probe frequency ω_p and the pump amplitude δ for $G(\omega_p/2\pi = 5 \text{ GHz}) = 2\pi \times 0.7 \text{ MHz}$. The qubit is irradiated by a pump with frequency (a) $\omega_{\text{pump}}/2\pi = 1 \text{ MHz}$, (b) $\omega_{\text{pump}}/2\pi = 5 \text{ MHz}$, (c) $\omega_{\text{pump}}/2\pi = 10 \text{ MHz}$. In (c), the drift on multi-photon resonance at high power is due to flux drift.

C. LZSM interferometry of the system in the stationary regime

In this subsection we give a brief comparison with previous related research, in Ref. [36]. The main difference between these two studies is that in the previous experiment the qubit was located in the node [blue curve in Fig. 1(a)], thus it was "hidden" or "decoupled" from the transmission line. In other words, the qubit was exposed to the electric field, but could not experience the electric field because the qubit was located at the node. By tuning the qubit to the node frequency, we could decouple the $k = 0$ sideband and see the other sidebands.

In this work, we tuned slightly away from the node frequency [red curve in Fig. 1(a)], and we see the time dynamics of the $k = 0$ photon-dressed resonance. The advantage of shifting slightly away from the node frequency is in obtaining a long coherence time $T_2 = 1/T_2 \sim 1/2\pi \times 0.75 \text{ MHz} \sim 212 \text{ ns}$ (see Table I), which is important to observe the time dynamics of the photon-dressed resonance, using a finite-time-resolution digitizer.

The time domain measurements were not made in Ref. [36], because the relaxation rate and pure dephasing rate were much higher than in the current work, where the qubit-transmission line coupling is intentionally designed to be weak. Regarding the relaxation time and pure dephasing time in Ref. [36], we could not resolve these with a finite bandwidth digitizer (5 ns resolution), because the dynamics was too fast.

Also, compared to the preceding work, the coupling capacitor to the transmission line is decreased because of the intended and desired weak coupling, where the relaxation rate is smaller and the coherence time is larger. This allows us to reveal the dynamics with a nano-second digitizer. In order to keep the same charging energy, which determines the anharmonicity, we have to increase the shunt capacitance to keep the same total capacitance.

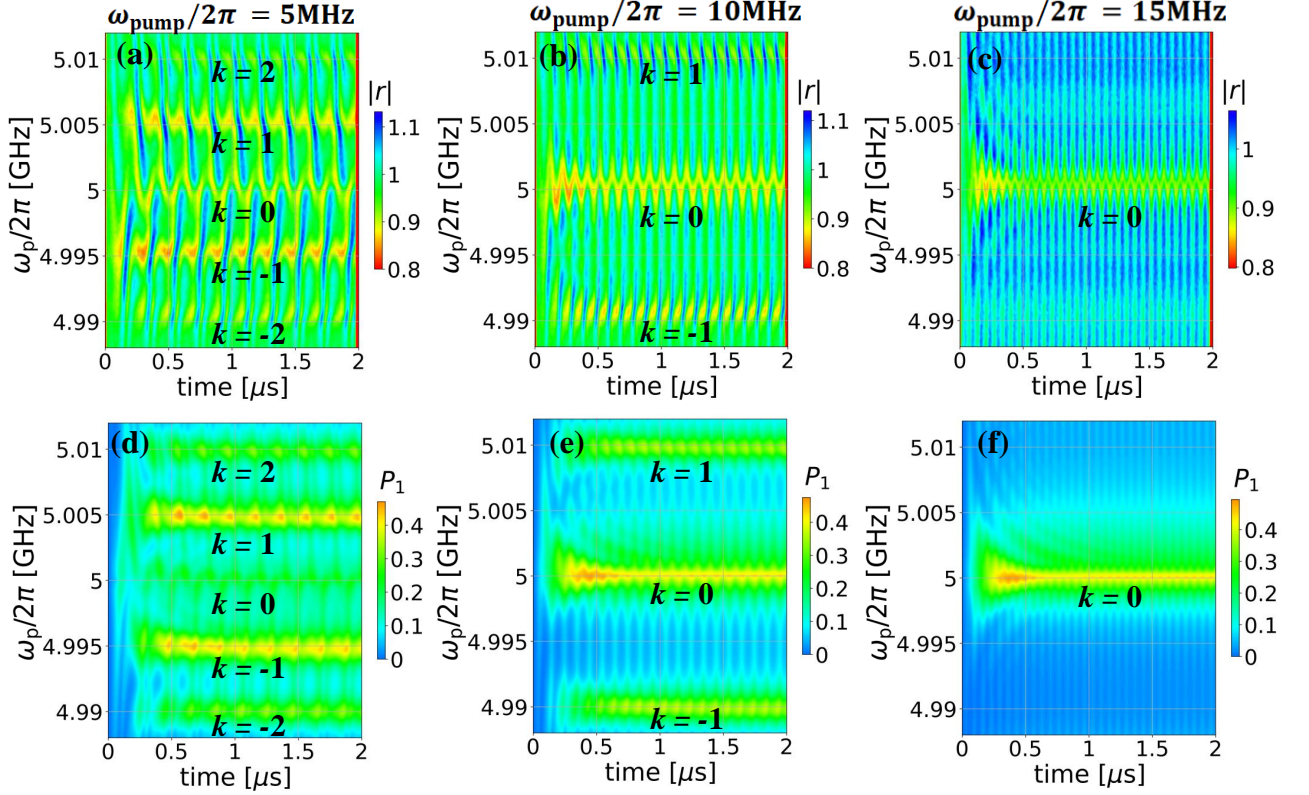


Figure 4: Coherent dynamics of the transmon qubit: dependence of the reflection coefficient $|r|$ (the upper-level occupation probability P_1) using the probe power $P_p = -146$ dBm [$G(\omega_p/2\pi) = 2\pi \times 1.4$ MHz] and the pump power $P_{\text{pump}} = -78.5$ dBm ($\delta = 10$ MHz) on the probe frequency ω_p and time t . Plots (a,b,c) present experimental results, (d,e,f) show plots built by data computed theoretically. The qubit is irradiated by a pump with frequency (a) $\omega_{\text{pump}}/2\pi = 5$ MHz, (b) $\omega_{\text{pump}}/2\pi = 10$ MHz, (c) $\omega_{\text{pump}}/2\pi = 15$ MHz. Panels (d-f) show the corresponding data computed theoretically for the qubit upper-level occupation probabilities P_1 .

D. Temporal dynamics of the atom-mirror under both pump and probe signals

We study the time dynamics of the atom-mirror system under both probe and dressing (pump) signals. In particular, we send a probe square pulse (Gaussian rise ~ 10 ns) to the transmission line and continuous sinusoidal wave pump to the on-chip flux line, see Fig. 1(f). We measure the reflection coefficient as a function of time and probe the frequency for a weak probe under the influence of a fixed pump power and fixed pump frequency.

In Fig. 4, each plot is taken at a fixed pump power $P_{\text{pump}} = -78.5$ dBm and pump frequency. Note that $\omega_{\text{pump}}/2\pi = 5$ MHz for panels (a,d); $\omega_{\text{pump}}/2\pi = 10$ MHz for panels (b, e); and $\omega_{\text{pump}}/2\pi = 15$ MHz for panels (c, f). The probe pulse starts at the beginning of the plot at $t = 0$. In Fig. 4 (a,b,c) the reflection coefficient reveals a transient dynamics starting at $t = 0$. This transient dynamics, affected by the initial conditions, ends up in a stationary solution, determined by the competition of driving and relaxation. In addition, we see the time dynamics of the multi-photon resonances, which occur at

$\Delta\omega = k\omega_{\text{pump}}$, labeled by $k = -2, -1, 0, +1, +2$. And the multi-photon resonances are slightly asymmetric around $k = 0$. All of these features are consistent with the theory described in Sec. III.

In Fig. 5, by taking line cuts of Fig. 4, we show detailed features of the transient dynamics at various fixed pump frequencies ω_{pump} . Moreover, in Fig. 6, we also fix the pump frequency to 10 MHz and vary the pump power in (a,b,c). We see the multi-photon resonances, occurring at $k = -1, +1$, becoming weaker and weaker from (a) to (c), as the pump power decreases.

In Fig. 5, we can see the line cut along Fig. 4 at $\omega_p/2\pi = 5$ GHz. For a clearer comparison between theory and experiment, the y -axis for the theoretical plots was cropped and inverted. We see the transient dynamics (oscillations with a frequency inversely proportional to the pump frequency ω_{pump}) around $T_2 = 1/\Gamma_2 \sim 212$ ns for $\omega_{\text{pump}}/2\pi = 15$ MHz, where $T_2 > 2\pi/\omega_{\text{pump}}$ in Fig. 5(c). When $T_2 \sim 2\pi/\omega_{\text{pump}}$, the transient dynamics is not clear, as shown in Fig. 5(a). In the steady state, the period of oscillations is the inverse of the pump frequency, as expected. The theory plots show the upper-level occupation probability P_1 , where the transient dynamics is

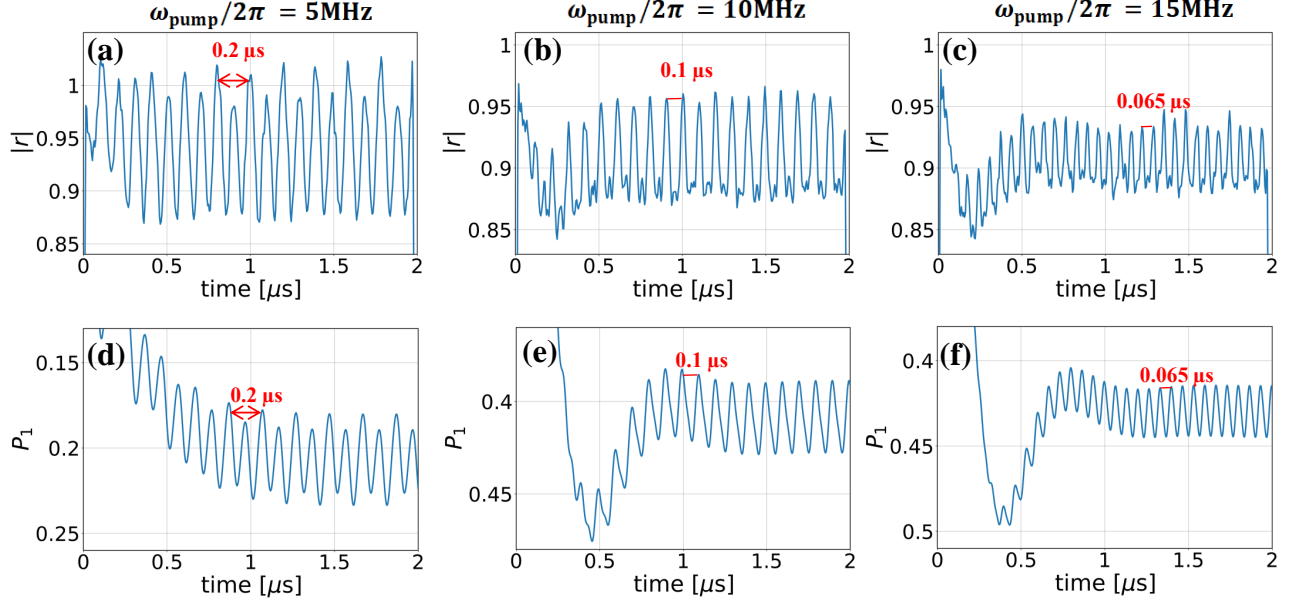


Figure 5: Line cut of Fig. 4 along $\omega_p/2\pi = 5$ GHz. Coherent dynamics of the transmon qubit: dependence of the reflection coefficient $|r|$ (the upper-level occupation probability P_1) on the time t at fixed pump frequency ω_{pump} with $\omega_p/2\pi = 5$ GHz, $P_p = -146$ dBm [$G(\omega_p/2\pi = 5 \text{ GHz}) = 2\pi \times 1.4 \text{ MHz}$], $P_{\text{pump}} = -78.5$ dBm ($\delta = 10 \text{ MHz}$). Plots (a,b,c) present experimental results, while panels (d,e,f) show plots computed theoretically. The qubit is irradiated by a signal with frequency (a) $\omega_{\text{pump}}/2\pi = 5 \text{ MHz}$, (b) $\omega_{\text{pump}}/2\pi = 10 \text{ MHz}$, (c) $\omega_{\text{pump}}/2\pi = 15 \text{ MHz}$. Panels (d,e,f) show the corresponding data computed theoretically for the qubit upper-level occupation probabilities P_1 . For a clearer comparison between theory and experiments, the y -axis of the theoretical plots in (d,e,f) were cropped and inverted.

around $T_1 = 1/\Gamma_1 \sim 568 \text{ ns}$. Also, for a better understanding of the qubit dynamics formation driven by the flux pump, we show the case when pump is off. From this, we learn that the features at $k = \pm 1$ disappear. The corresponding plots are presented in Fig. 7 in the Appendix.

III. THEORETICAL DESCRIPTION

In Ref. [36], the experimentally measured reflection coefficient $|r|$ is associated with the theoretically calculated probability of an upper level occupation P_1 (increasing P_1 corresponds to decreasing $|r|$). The computations were done in the diabatic (charge) basis. Here we use the same correspondence between theory and experiment and make our calculations in the diabatic basis. The system can be described by the Hamiltonian:

$$H = -\frac{B_z}{2}\sigma_z - \frac{B_x}{2}\sigma_x, \quad (2)$$

where the diagonal part corresponds to the energy-level modulation

$$B_z/\hbar = \omega_{10} + \delta \sin \omega_{\text{pump}} t, \quad (3)$$

the off-diagonal part characterizes the coupling to the probe signal

$$B_x/\hbar = G \sin \omega_p t. \quad (4)$$

To remove the fast driving from the Hamiltonian, Ref. [36] considered the unitary transformation $U = \exp(-i\omega_p \sigma_z t/2)$ and the rotating-wave approximation [39, 40] to obtain the new Hamiltonian

$$H_1 = -\frac{\hbar \widetilde{\Delta\omega}}{2}\sigma_z + \frac{\hbar G}{2}\sigma_x, \quad (5)$$

where

$$\widetilde{\Delta\omega} = \Delta\omega + f(t), \quad (6)$$

$$\Delta\omega = \omega_p - \omega_{10}, \quad (7)$$

$$f(t) = \delta \sin \omega_{\text{pump}} t. \quad (8)$$

Here δ is the amplitude of the energy-level modulation, G characterizes the coupling to the probe signal (Rabi frequency of the probe signal). According to Ref. [36]

$$G = \frac{\omega_p - \omega_{\text{node}}}{\omega_{\text{node}}} G_0, \quad (9)$$

where ω_{node} describes the qubit position in a semi-infinite transmission line [corresponding to the blue curve in Fig. 1(a)], and G_0 is proportional to the probe signal amplitude. Such a dependence causes the asymmetry about the line $\omega_p/2\pi = 5 \text{ GHz}$ in Figs. 3, 4, 6. For the current experiment $\omega_{\text{node}}/2\pi = 4.38 \text{ GHz}$. For any multi-photon resonance close to the node frequency, the linewidth will be narrower. The closer it is, the narrower it is. Therefore, it gives the asymmetry about the qubit resonance at

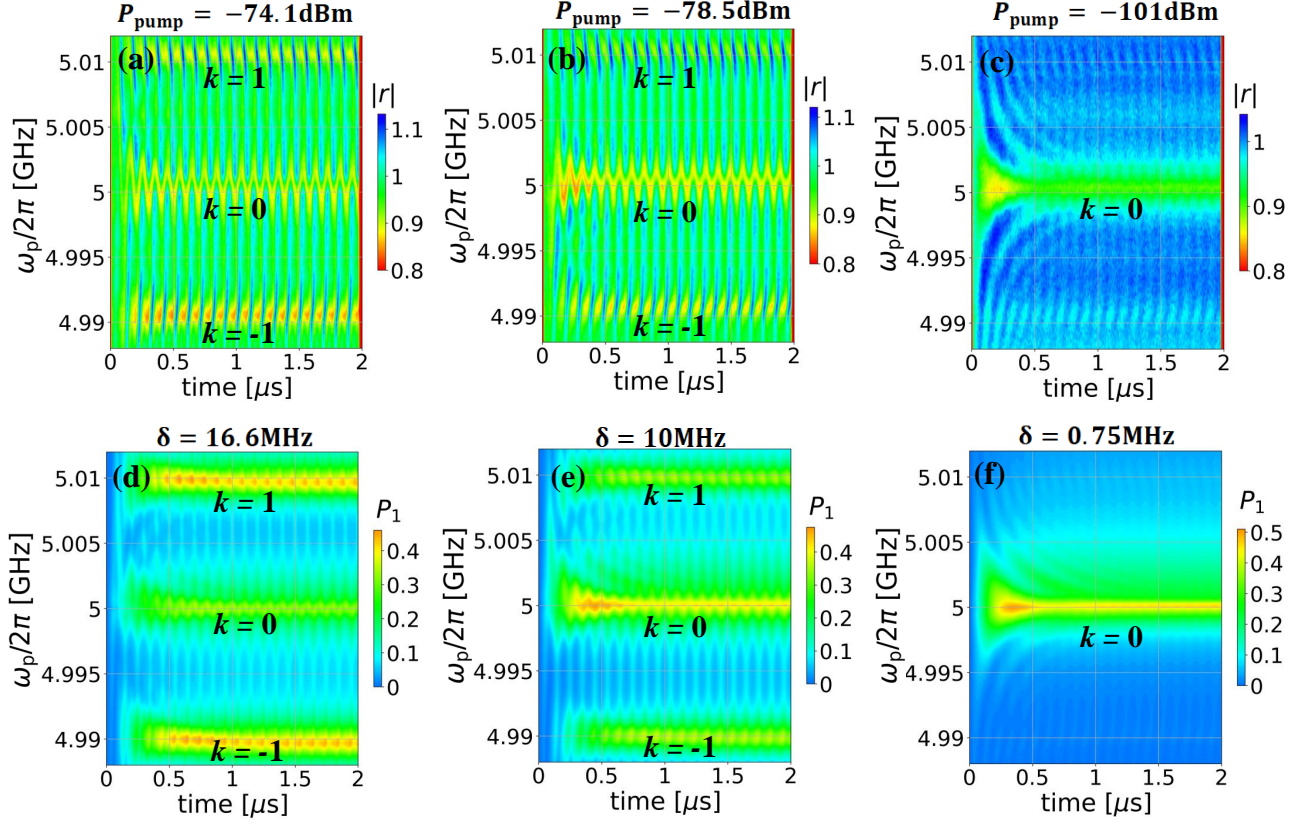


Figure 6: Coherent dynamics of the transmon qubit: dependence of the reflection coefficient $|r|$ (the upper-level occupation probability P_1) versus time t , using the probe power $P_p = -146$ dBm [$G(\omega_p/2\pi = 5 \text{ GHz}) = 2\pi \times 1.4 \text{ MHz}$ for the theory] on the probe frequency $\omega_p/2\pi$. Plots (a,b,c) present experimental results; while (d,e,f) show plots built by data computed theoretically. The qubit is irradiated by a pump signal with frequency $\omega_{\text{pump}}/2\pi = 10 \text{ MHz}$ and power (a) $P_{\text{pump}} = -74.1 \text{ dBm}$, (b) $P_{\text{pump}} = -78.5 \text{ dBm}$, (c) $P_{\text{pump}} = -101 \text{ dBm}$. The theoretical results from the qubit upper-level occupation probability P_1 are shown for $\delta = 16.6 \text{ MHz}$ in (d), for $\delta = 10 \text{ MHz}$ in (e), and for $\delta = 0.75 \text{ MHz}$ in (f).

$\omega_p/2\pi = 5 \text{ GHz}$. Moreover, one can see that if $\omega_p = \omega_{\text{node}}$ the qubit is “hidden” or “decoupled” from the transmission line, with $G = 0$.

In order to describe the qubit dynamics, we use the Lindblad equation, which in the diabatic basis with the Hamiltonian (5) has the form:

$$\frac{d\rho}{dt} = -\frac{i}{\hbar} [\hat{H}_1, \rho] + \sum_{\alpha} \check{L}_{\alpha}[\rho], \quad (10)$$

where $\rho = \begin{pmatrix} \rho_{00} & \rho_{01} \\ \rho_{01}^* & 1 - \rho_{00} \end{pmatrix}$ is the density matrix, such that $P_1 = 1 - \rho_{00}$. The Lindblad superoperator \check{L}_{α} characterizes the system relaxation caused by interactions with the environment,

$$\check{L}_{\alpha}[\rho] = L_{\alpha}\rho L_{\alpha}^{\dagger} - \frac{1}{2} \{L_{\alpha}^{\dagger}L_{\alpha}, \rho\}, \quad (11)$$

where $\{a, b\} = ab + ba$ is the anticommutator. For a qubit there are two possible relaxation channels: energy relaxation (described by L_{relax}) and dephasing (described by L_{ϕ}). The corresponding operators can be expressed

in the following form:

$$L_{\text{relax}} = \sqrt{\Gamma_1}\sigma^+, \quad L_{\phi} = \sqrt{\frac{\Gamma_{\phi}}{2}}\sigma_z \quad (12)$$

with $\sigma^+ = \begin{pmatrix} 0 & 1 \\ 0 & 0 \end{pmatrix}$, $\sigma_z = \begin{pmatrix} 1 & 0 \\ 0 & -1 \end{pmatrix}$, Γ_1 being the qubit relaxation, $\Gamma_2 = \Gamma_1/2 + \Gamma_{\phi}$ is the decoherence rate, Γ_{ϕ} is the pure dephasing rate.

IV. INTERFEROMETRY AND DYNAMICS

By solving Eq. (10) we obtain P_1 as a function of time t , pump frequency ω_{pump} , pump power P_{pump} (which corresponds to δ in theory), probe frequency ω_p , probe power P_p (which corresponds to G in theory). The occupation probability is the function of all these parameters, $P_1 = P_1(t, \omega_{\text{pump}}, \omega_p, \delta, G)$. The dependence obtained allows us to build, for instance, $P_1 = P_1(\omega_p, t)$. Also we can compute the dependencies for P_1 in a stationary regime by making the time averaging of the results.

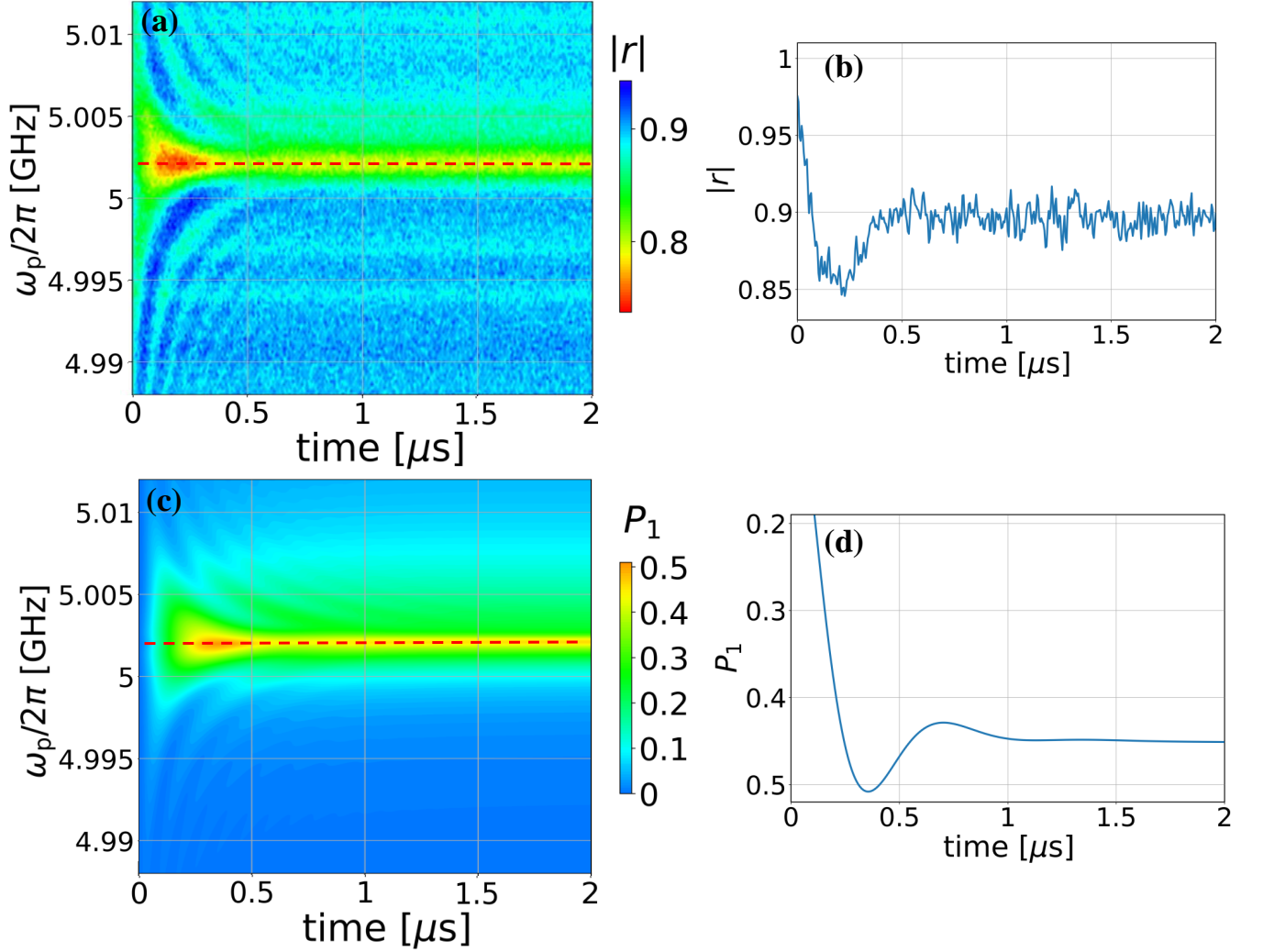


Figure 7: Coherent dynamics of the transmon qubit: dependence of the reflection coefficient $|r|$ (the upper-level occupation probability P_1) with pump off on the probe frequency ω_p and time t for a weak probe $P_p = -146$ dBm [$G(\omega_p/2\pi = 5 \text{ GHz}) = 2\pi \times 1.4 \text{ MHz}$] and $\omega_{10}/2\pi = 5.002 \text{ GHz}$. Plots (a, b) present experimental results; while (c, d) show plots computed theoretically. Panels (b) and (d) are line cuts of the experimental (a) and theoretical (c) plots, respectively, at $\omega_p/2\pi = 5.002 \text{ GHz}$.

Figure 3 shows a time-averaged interferogram, where P_1 is a function of δ and ω_p . We use the extracted parameters in Fig. 2, and select $G(\omega_p/2\pi = 5 \text{ GHz}) = 2\pi \times 0.7 \text{ MHz}$ in Fig. 3; $G(\omega_p/2\pi = 5 \text{ GHz}) = 2\pi \times 1.4 \text{ MHz}$ in Figs. 4, 5, 6, 7 (the calibration between Rabi frequency and power, data is not shown) for the theory plots.

For obtaining time-averaged values, we analyzed the curve $P_1 = P_1(t)$ to extract the minimal time t_{\min} after which the oscillation amplitude has no change. And then applied averaging for the interval $[t_{\min}, t_{\text{final}}]$, where t_{final} corresponds to the time of the pulse turning off. We determined that for our case $t_{\min} = 1.5 \mu\text{s}$ and $t_{\text{final}} = 2.0 \mu\text{s}$.

Such interferograms are useful not only for obtaining the fitting parameters, but also they play a key role for characterizing the system. Particularly, such kind of figures:

- allow to estimate the decoherence time of the system. Consider cases (a) and (b) of Fig. 3. We see that for the case (b) the peaks are separated, while for (a) they are not distinguishable. The maximal frequency ω_{pump} for which we have a blurred picture (when individual resonances are not distinguishable) corresponds to the system decoherence time. So, one can conclude that $\Gamma_2/2\pi \simeq 1 \text{ MHz}$;
- provide a tool for power calibration by interrelating the unknown distance between the zeros along the vertical axis in the experiment with the zeros of the Bessel function in theory;
- provide novel opportunities for multi-photon spectroscopy. The resonances appear when $\omega_p = \omega_{10} \pm k\omega_{\text{pump}}$, where k is an integer number. Or, in other words, the system is resonantly excited when the

dressed qubit energy gap is equal to the energy of k photons, $k\hbar\omega_{\text{pump}}$ [36].

In order to see the qubit dynamics we built the dependence $P_1 = P_1(\omega_p, t)$ for different pump frequencies $\omega_{\text{pump}}/2\pi = 5$ MHz, 10 MHz, 15 MHz in Fig. 4. As expected, for the stationary case, the resonances are observed at $\omega_p = \omega_{10} \pm k\omega_{\text{pump}}$, and the value of the reflection coefficient $|r|$ (occupation probability P_1) oscillates with period $T = 2\pi/\omega_{\text{pump}}$.

All theoretical plots were built by solving the Lindblad equation within the framework QUTIP (Quantum Toolbox in PYTHON) [41, 42]. The function `mesolve($H, \rho_0, c_{\text{ops}}, \dots$)` from this library takes the Hamiltonian H in a matrix form (in our case $H = H_1$), the initial state of the system ρ_0 (we assume that initially the system is in the ground state $|0\rangle$), the set of collapse operators c_{ops} which are related to the Lindblad superoperators (11) and some other parameters. The function `mesolve($H, \rho_0, c_{\text{ops}}, \dots$)` returns elements of the density matrix ρ dependent on time.

V. CONCLUSIONS

We considered the dynamics and stationary regime of a capacitively shunted transmon-type qubit in front of a mirror, affected by two signals: probe and dressing (pump) signals. The multi-photon resonance dynamics, occurring at $\omega_p = \omega_{10} \pm k\omega_{\text{pump}}$, consists of two temporal regimes: transient and stationary. In particular, we observed the dynamics of $k = 0, \pm 1, \pm 2$ multi-photon resonances, because the node frequency is away from those resonances. The occupation probability P_1 obtained with the Lindblad equation and the experimentally measured reflection coefficient $|r|$ agree well with each other. Taking advantages of the strong coupling between the propagating field and qubit, and the ease of fabrication, superconducting qubits in front of a mirror provide a clear platform to study the dynamics of LZSM interference compared with other quantum two-level system [43].

Acknowledgments

I.-C.H. acknowledges financial support from the Research Grants Council of Hong Kong (Grant No. 11312322). J.C.C. acknowledges financial support from the NSTC of Taiwan under project 110-2112-M-007 - 022 -MY3 and 111-2119-M-007 -008. P.Y.W. acknowledges financial support from the NSTC of Taiwan under project 110-2112-M-194-006-MY3. M.P.L. and S.N.S. were supported by Army Research Office (ARO) (Grant

No. W911NF2010261). F.N. is supported in part by: Nippon Telegraph and Telephone Corporation (NTT) Research, the Japan Science and Technology Agency (JST) [via the Quantum Leap Flagship Program (Q-LEAP)], and the Moonshot R&D Grant Number JPMJMS2061], the Asian Office of Aerospace Research and Development (AOARD) (via Grant No. FA2386-20-1-4069), and the Foundational Questions Institute Fund (FQXi) via Grant No. FQXi-IAF19-06.

Appendix A: Time dynamics of an atom-mirror system irradiated by probe and dressing (pump) signals

Here we consider one more case of studying the time dynamics of the atom-mirror system irradiated by probe and dressing (pump) signals. One possible approach involves fixing the probe frequency ω_p and analyzing the reflection coefficient $|r|$ as function of time t , as shown in Fig. 5. The measurements and calculations were done for various values of the pump frequency $\omega_{\text{pump}}/2\pi = 5$ MHz, 10 MHz, 15 MHz, with $\omega_p/2\pi = 5$ GHz. From the analysis of the plots one could conclude that:

- the probability and the reflection coefficient oscillate with period $T = 2\pi/\omega_{\text{pump}}$;
- for the pumping frequency, $\omega_{\text{pump}}/2\pi = 5$ MHz, there are two kinds of peaks: high and low ones;
- the system dynamics consists of two regimes: stationary and transient ones. The stationary regime is observed after $t = 1.5 \mu\text{s}$ for all the cases considered.

Figure 6 shows the dependence of the reflection coefficient $|r|$ as a function of the probe frequency ω_p and time t . The measurements and calculations were done for various values of the pump power P_{pump} (δ in the theory) and fixed pump frequency $\omega_{\text{pump}}/2\pi = 10$ MHz. From the plots we can deduce that increasing the pump power amplifies the resonances.

To understand better the influence of the pump signal on the system dynamics, we also show the plots with no flux pump. The corresponding results with $\delta = 0$ and $\omega_{10}/2\pi = 5.002$ GHz (in this case ω_{10} is slightly changed due to a slightly different flux bias) are shown in Fig. 7. Panel (a) shows the dependence of the reflection coefficient $|r|$ on time t and probe frequency ω_p , (c) is the corresponding theoretical result; panel (b) is the line cut of (a) at $\omega_p/2\pi = 5.002$ GHz, and (d) is the corresponding theoretical curve.

* These authors contributed equally to this work

† e-mail: sshevchenko@ilt.kharkov.ua

‡ e-mail: iochoi@cityu.edu.hk

¹ M. A. Nielsen and I. L. Chuang, *Quantum Computa-*

- tion and Quantum Information: 10th Anniversary Edition* (Cambridge University Press, 2010).
- ² H. Haffner, C. Roos, and R. Blatt, “Quantum computing with trapped ions,” *Phys. Rep.* **469**, 155–203 (2008).
 - ³ F. Arute *et al.*, “Quantum supremacy using a programmable superconducting processor,” *Nature* **574**, 505 (2019).
 - ⁴ I. Buluta, S. Ashhab, and F. Nori, “Natural and artificial atoms for quantum computation,” *Rep. Prog. Phys.* **74**, 104401 (2011).
 - ⁵ M. Kjaergaard, M. E. Schwartz, J. Braumüller, P. Krantz, J. I.-J. Wang, S. Gustavsson, and W. D. Oliver, “Superconducting qubits: Current state of play,” *Annu. Rev. Condens. Matter Phys.* **11**, 369 (2020).
 - ⁶ A. F. Kockum and F. Nori, “Quantum Bits with Josephson Junctions,” in *Fundamentals and Frontiers of the Josephson Effect* (Springer International Publishing, 2019) pp. 703–741.
 - ⁷ X. Gu, A. F. Kockum, A. Miranowicz, Y.-X. Liu, and F. Nori, “Microwave photonics with superconducting quantum circuits,” *Phys. Rep.* **718-719**, 1–102 (2017).
 - ⁸ J. M. Gambetta, J. M. Chow, and M. Steffen, “Building logical qubits in a superconducting quantum computing system,” *npj Quantum Information* **3**, 2 (2017).
 - ⁹ C. Wang *et al.*, “Towards practical quantum computers: transmon qubit with a lifetime approaching 0.5 milliseconds,” *npj Quantum Information* **8**, 3 (2022).
 - ¹⁰ W. D. Oliver and P. B. Welander, “Materials in superconducting quantum bits,” *MRS Bulletin* **38**, 816 (2013).
 - ¹¹ I.-C. Hoi, A. F. Kockum, L. Tornberg, A. Pourkabirian, G. Johansson, P. Delsing, and C. M. Wilson, “Probing the quantum vacuum with an artificial atom in front of a mirror,” *Nat. Phys.* **11**, 1045–1049 (2015).
 - ¹² K. Lalumière, B. C. Sanders, A. F. van Loo, A. Fedorov, A. Wallraff, and A. Blais, “Input-output theory for waveguide QED with an ensemble of inhomogeneous atoms,” *Phys. Rev. A* **88**, 043806 (2013).
 - ¹³ A. Blais, S. M. Girvin, and W. D. Oliver, “Quantum information processing and quantum optics with circuit quantum electrodynamics,” *Nat. Phys.* **16**, 247–256 (2020).
 - ¹⁴ B. Kannan, M. J. Ruckriegel, D. L. Campbell, A. F. Kockum, J. Braumüller, D. K. Kim, M. Kjaergaard, P. Krantz, A. Melville, B. M. Niedzielski, A. Vepsäläinen, R. Winik, J. L. Yoder, F. Nori, T. P. Orlando, S. Gustavsson, and W. D. Oliver, “Waveguide quantum electrodynamics with superconducting artificial giant atoms,” *Nature* **583**, 775–779 (2020).
 - ¹⁵ P. Y. Wen, A. F. Kockum, H. Ian, J. C. Chen, F. Nori, and I.-C. Hoi, “Reflective amplification without population inversion from a strongly driven superconducting qubit,” *Phys. Rev. Lett.* **120**, 063603 (2018).
 - ¹⁶ X. Xu, B. Sun, P. R. Berman, D. G. Steel, A. S. Bracker, D. Gammon, and L. J. Sham, “Coherent optical spectroscopy of a strongly driven quantum dot,” *Science* **317**, 929–932 (2007).
 - ¹⁷ F. Y. Wu, S. Ezekiel, M. Ducloy, and B. R. Mollow, “Observation of amplification in a strongly driven two-level atomic system at optical frequencies,” *Phys. Rev. Lett.* **38**, 1077–1080 (1977).
 - ¹⁸ M. Mirhosseini, E. Kim, X. Zhang, A. Sipahigil, P. B. Dieterle, A. J. Keller, A. Asenjo-Garcia, D. E. Chang, and O. Painter, “Cavity quantum electrodynamics with atom-like mirrors,” *Nature* **569**, 692 (2019).
 - ¹⁹ P. Y. Wen, K.-T. Lin, A. F. Kockum, B. Suri, H. Ian, J. C. Chen, S. Y. Mao, C. C. Chiu, P. Delsing, F. Nori, G.-D. Lin, and I.-C. Hoi, “Large collective Lamb shift of two distant superconducting artificial atoms,” *Phys. Rev. Lett.* **123**, 233602 (2019).
 - ²⁰ I.-C. Hoi, T. Palomaki, J. Lindkvist, G. Johansson, P. Delsing, and C. M. Wilson, “Generation of nonclassical microwave states using an artificial atom in 1D open space,” *Phys. Rev. Lett.* **108**, 263601 (2012).
 - ²¹ C. M. Wilson, G. Johansson, A. Pourkabirian, M. Simoen, J. R. Johansson, T. Duty, F. Nori, and P. Delsing, “Observation of the dynamical Casimir effect in a superconducting circuit,” *Nature* **479**, 376–379 (2011).
 - ²² I.-C. Hoi, A. F. Kockum, T. Palomaki, T. M. Stace, B. Fan, L. Tornberg, S. R. Sathyamoorthy, G. Johansson, P. Delsing, and C. M. Wilson, “Giant Cross-Kerr effect for propagating microwaves induced by an artificial atom,” *Phys. Rev. Lett.* **111**, 053601 (2013).
 - ²³ I.-C. Hoi, C. M. Wilson, G. Johansson, T. Palomaki, B. Peropadre, and P. Delsing, “Demonstration of a single-photon router in the microwave regime,” *Phys. Rev. Lett.* **107**, 073601 (2011).
 - ²⁴ D. Karpov, V. Monarkha, D. Szombati, A. Frieiro, A. Omelyanchouk, E. Il’ichev, A. Fedorov, and S. Shevchenko, “Probabilistic motional averaging,” *Eur. Phys. J. B* **93**, 49 (2020).
 - ²⁵ W. D. Oliver, Y. Yu, J. C. Lee, K. K. Berggren, L. S. Levitov, and T. P. Orlando, “Mach-Zehnder interferometry in a strongly driven superconducting qubit,” *Science* **310**, 1653–1657 (2005).
 - ²⁶ M. Sillanpää, T. Lehtinen, A. Paila, Y. Makhlin, and P. Hakonen, “Continuous-time monitoring of Landau-Zener interference in a Cooper-pair box,” *Phys. Rev. Lett.* **96**, 187002 (2006).
 - ²⁷ S. N. Shevchenko, S. Ashhab, and F. Nori, “Landau-Zener-Stückelberg interferometry,” *Phys. Rep.* **492**, 1–30 (2010).
 - ²⁸ O. V. Ivakhnenko, S. N. Shevchenko, and F. Nori, “Nonadiabatic Landau-Zener-Stückelberg-Majorana transitions, dynamics and interference,” *Phys. Rep.* **995**, 1–89 (2023).
 - ²⁹ L. Y. Gorelik, N. I. Lundin, V. S. Shumeiko, R. I. Shekhter, and M. Jonson, “Superconducting single-mode contact as a microwave-activated quantum interferometer,” *Phys. Rev. Lett.* **81**, 2538–2541 (1998).
 - ³⁰ T. Wu, Y. Zhou, Y. Xu, S. Liu, and J. Li, “Landau-Zener-Stückelberg interference in nonlinear regime,” *Chin. Phys. Lett.* **36**, 124204 (2019).
 - ³¹ S. N. Shevchenko, *Mesoscopic Physics meets Quantum Engineering* (World Scientific, Singapore, 2019).
 - ³² P. O. Kofman, O. V. Ivakhnenko, S. N. Shevchenko, and F. Nori, “Majorana’s approach to nonadiabatic transitions validates the adiabatic-impulse approximation,” *Sci. Rep.* **13**, 5053 (2023).
 - ³³ M. P. Liul and S. N. Shevchenko, “Rate-equation approach for multi-level quantum systems,” *Low Temp. Phys.* **49**, 102–108 (2023).
 - ³⁴ A. M. Satanin, M. V. Denisenko, S. Ashhab, and F. Nori, “Amplitude spectroscopy of two coupled qubits,” *Phys. Rev. B* **85**, 184524 (2012).
 - ³⁵ D. L. Campbell, Y.-P. Shim, B. Kannan, R. Winik, D. K. Kim, A. Melville, B. M. Niedzielski, J. L. Yoder, C. Tahan, S. Gustavsson, and W. D. Oliver, “Universal nonadiabatic control of small-gap superconducting qubits,” *Phys. Rev. X* **10**, 041051 (2020).
 - ³⁶ P. Y. Wen, O. V. Ivakhnenko, M. A. Nakonechnyi, B. Suri,

- J.-J. Lin, W.-J. Lin, J. C. Chen, S. N. Shevchenko, F. Nori, and I.-C. Hoi, “Landau-Zener-Stückelberg-Majorana interferometry of a superconducting qubit in front of a mirror,” *Phys. Rev. B* **102**, 075448 (2020).
- ³⁷ W.-J. Lin *et al.*, “Deterministic loading of microwaves onto an artificial atom using a time-reversed waveform,” *Nano Lett.* **22**, 8137–8142 (2022).
- ³⁸ S. Probst, F. B. Song, P. A. Bushev, A. V. Ustinov, and M. Weides, “Efficient and robust analysis of complex scattering data under noise in microwave resonators,” *Rev. Sci. Instrum.* **86**, 024706 (2015).
- ³⁹ M. Silveri, K. Kumar, J. Tuorila, J. Li, A. Vepsäläinen, E. Thuneberg, and G. Paraoanu, “Stueckelberg interference in a superconducting qubit under periodic latching modulation,” *New J. Phys.* **17**, 043058 (2015).
- ⁴⁰ K. Ono, S. N. Shevchenko, T. Mori, S. Moriyama, and F. Nori, “Analog of a quantum heat engine using a single-spin qubit,” *Phys. Rev. Lett.* **125**, 166802 (2020).
- ⁴¹ J. Johansson, P. Nation, and F. Nori, “QuTiP: An open-source Python framework for the dynamics of open quantum systems,” *Comput. Phys. Commun.* **183**, 1760–1772 (2012).
- ⁴² J. Johansson, P. Nation, and F. Nori, “QuTiP 2: A Python framework for the dynamics of open quantum systems,” *Comput. Phys. Commun.* **184**, 1234–1240 (2013).
- ⁴³ A. Bogan, S. Studenikin, M. Korkusinski, L. Gaudreau, P. Zawadzki, A. S. Sachrajda, L. Tracy, J. Reno, and T. Hargett, “Landau-Zener-Stückelberg-Majorana interferometry of a single hole,” *Phys. Rev. Lett.* **120**, 207701 (2018).